Interferon-γ is a direct driver of crypt hyperplasia in celiac disease

Jorunn Stamnaes[1,2,3*], Daniel Stray[1], M. Fleur du Pré[1,3], Louise F. Risnes[1,4], Alisa E. Dewan[1,3], Jakeer Shaik[3], Maria Stensland[2], Knut E. A. Lundin[1,4], Ludvig M. Sollid[1,3 *]

[1] Norwegian Coeliac Disease Research Centre, Institute of Clinical Medicine, University of Oslo, Oslo, Norway

[2] Proteomics Core Facility, University of Oslo and Oslo University Hospital, Oslo, Norway

[3] Department of Immunology, Oslo University Hospital-Rikshospitalet, Oslo, Norway

[4] Department of Gastroenterology, Oslo University Hospital-Rikshospitalet, Oslo, Norway

[*] Correspondence to:

Ludvig M. Sollid

l.m.sollid@medisin.uio.no

Jorunn Stamnaes

jorunn.stamnas@medisin.uio.no

Department of Immunology, Oslo University Hospital-Rikshospitalet, NO-0372, Oslo, Norway

P: +47 23073811

F: +47 23073510

Conflict of interest: The authors have declared that no conflict of interest exists.

Key Words: crypt hyperplasia, interferon-gamma, small intestine, celiac disease

Abstract

Crypt hyperplasia is a key feature of celiac disease and several other small intestinal inflammatory conditions. Analysis of the gut epithelial crypt zone by mass spectrometry-based tissue proteomics revealed a strong interferon-γ (IFN-γ) signal in active celiac disease. This signal, hallmarked by increased expression of MHC molecules, was paralleled by diminished expression of proteins associated with fatty acid metabolism. Crypt hyperplasia and the same proteomic changes were observed in wild type mice administered IFN-γ. In mice with conditional knockout of the IFN-γ receptor in gut epithelial cells these signature morphological and proteomic changes were not induced on IFN-γ administration. IFN-γ is thus a driver of crypt hyperplasia in celiac disease by acting directly on crypt epithelial cells. The results are relevant to other enteropathies with involvement of IFN-γ.

Introduction

Crypt hyperplasia in the small intestine with elongation of the crypts of Lieberkühn is a pathological tissue alteration commonly seen in inflammatory conditions (1, 2). It is accompanied by increased epithelial cell turnover, and also, when there is protracted inflammation, by blunting of the intestinal villi. In the intestine Lgr5+ intestinal stem cells (ISCs) at the crypt base produce daughter cells that undergo proliferation in the transit amplifying zone (3). The generated cells move along the crypt-villous axis and differentiate before they eventually are shed at the villous tip. Under normal physiological conditions in the small intestine of humans the transit time from cell generation to cell expulsion is 3-5 days (4, 5). This transit process accelerates during inflammation resulting in the increased cell turnover. Reflecting the increased cell turnover in crypt hyperplasia, the number of proliferating cells is augmented, and the proliferating cells can be detected by staining for Ki67 or by labeling of newly synthesized DNA.

Perhaps the most notable condition hallmarked by crypt hyperplasia and villous blunting is celiac disease (CeD). This disease is a prevalent enteropathy caused by a maladapted immune response to cereal gluten proteins, and the condition is treated with a life-long strict gluten-free diet (6). The disease lesion is localized in the proximal small intestine, and the full-blown lesion has blunting of the villi (7), a threefold increase in proliferating cells per crypt (8) and the enterocyte turnover time is reduced to 24 hours (9). The drivers of the immune response to gluten in CeD are CD4+ T cells which recognize deamidated gluten peptides in the context of disease-associated HLA-DQ allotypes (10). These CD4+ T cells are located in the lamina propria (11) which fits with the observation that intraepithelial CD4+ T cells are scarce in man (12). The gluten-specific CD4+ T cells have a distinct phenotype (13) and a characteristic cytokine profile dominated by production of interferon-γ (IFN-γ) (14, 15). Intraepithelial CD8+ T cells also produce IFN-γ in active CeD (16, 17). Reflecting these observations, both proteomic and transcriptomic analyses of active celiac lesion tissue reveal clear signatures of IFN-γ influence (18, 19). In line with the typical intestinal tissue remodeling of CeD, the diagnosis is conventionally made by histological examination of small intestinal biopsies with scoring according to the Marsh-Oberhuber scale (Marsh 0, 1, 2, 3 a-c) (20). Marsh grades 2 and 3 both show presence of crypt hyperplasia, while Marsh 3a-c grades in addition have increasing degrees of villous blunting and are considered diagnostic for CeD (21).

Two distinct models have been presented to explain the crypt hyperplasia and increased epithelial turnover in CeD. One model explains the crypt hyperplasia as a mechanism compensatory to increased epithelial cells killing by intraepithelial lymphocytes. Both intraepithelial CD8+ T cells carrying αβ T-cell receptors (TCRs) and TCR γδ T cells have a cytotoxic potential that involve natural killer cell receptors recognizing stress induced molecules expressed by epithelial cells (22-24). These T cells are likely responsible for an increased epithelial cell killing observed in active CeD (25). The alternative model explains crypt hyperplasia as a consequence of increased crypt cell division following activation of T cells. It was demonstrated that activation of lamina propria CD4+ T cells leads to crypt hyperplasia (26, 27) and subsequently it was shown that cytokines produced by CD4+ T cells induce lamina propria fibroblasts to produce keratinocyte growth factor which acts on crypt cells to instigate increased cell division (28, 29). This model puts the primary driver of crypt hyperplasia at the level of stem cells, yet with cytokines produced by the CD4+ T cells acting on these cells indirectly via fibroblasts. The two models are not mutually exclusive. Understanding the basis for crypt hyperplasia is important not only for understanding the molecular underpinnings of CeD, but also for understanding the cellular programs of the small intestine that are activated by inflammatory cues.

Spatial tissue proteomics is a powerful technology which can elucidate disease mechanisms as recently demonstrated with toxic epidermal necrolysis (30). Here, we have used this technology on the crypt zone of intestinal biopsy sections of CeD patients followed consecutively from having active disease to being in remission on a gluten-free diet. Accompanied by interventional studies in genetically modified mice, the results demonstrate that IFN-γ is a driver of crypt hyperplasia in CeD by acting directly on crypt epithelial cells. Further, the results show that IFN-γ profoundly changes the metabolism of epithelial cells of the crypt zone. These findings have relevance for other inflammatory conditions of the gut where IFN-γ is a central cytokine.

Results

The crypt compartment proteome of the celiac small intestine

We analyzed archival formalin fixed paraffin embedded (FFPE) biopsies of twenty adult, untreated CeD patients (UCeD) both at the time of diagnosis (histology Marsh 3a-c) and in complete histological remission after treatment with gluten-free diet (treated CeD; TCeD; histology Marsh 0). The Marsh scoring was based on routine histology assessments. For comparison we included from our archival research biobank biopsies of 20 non-CeD subjects (controls; Ctr) with normal gut histology (31) (Supplemental Table 1). Tissue sections were stained with hematoxylin and azophloxin to identify Paneth cell granules to ensure correct identification of well oriented crypts, followed by laser capture microdissection of regions encompassing Paneth cells, ISCs and newly divided daughter cells (Figure 1A, and Supplemental Figure 1). Two replicate samples of pooled crypt regions were collected for all biopsies where possible (n = 109) and processed for mass spectrometry (MS) based proteomics analysis for protein identification and label-free quantification (Supplemental Table 2).

The crypt proteome in UCeD differs from that of TCeD and non-CeD controls

Principle component analysis (PCA) based on the expression of 1329 proteins revealed that crypt samples from UCeD biopsies differed from TCeD and Ctr samples (Figure 1B). Key drivers of the separation along PC1 included proteins indicative of inflammatory response such as STAT1, TAP1/TAP2, CD74, HLA-A and HLA-DRA as well as cell metabolism proteins such as HMGCS2, FABP1, RBP2 and AKR1B10 (Figure 1C). These proteins were also among the most significant differentially expressed proteins (DEPs) when comparing UCeD samples to Ctr samples (Two-sample Student's t-test; total n = 230; up in UCeD n = 134, down in UCeD n = 96) (Supplemental Table 3) (Figure 1D). Only thirteen proteins reached statistical significance when comparing TCeD and Ctr samples. However, the majority of proteins that were significantly changed in UCeD vs Ctr (DEP) showed similar directional fold change when comparing TCeD and Ctr samples (Figure 1E). This suggests varying degrees of low-level gut disease activity in the crypt of TCeD biopsies, which agrees with the positioning of TCeD samples between Ctr and UCeD samples in the PCA plot (Figure 1B). A notable exception was HMGCS2 which was similar in TCeD and Ctr samples. The key drivers of separation along PC1 were also among the most differentially expressed proteins. This significance held true when comparing expression in the level of individual proteins and biopsies (Figure 1F, G). Among the DEPs were IGHA1 which is not expressed by epithelial cells but is transported through epithelial cells via the poly Ig (PIGR) receptor. Indeed, both IGHA and IGJ signal correlated with PIGR expression (Figure 1H). Collectively, these data show that the crypt compartment proteome in CeD biopsies differs markedly from non-CeD controls with differential expression of proteins indicative of inflammation and altered metabolic profile.

The proteomic signatures of UCeD crypt compartment reveal response to IFN-γ and altered fatty acid metabolism

To determine the biological processes behind the differential proteome expression of UCeD crypts, we performed enrichment of biological pathways along PC1 (Supplemental Table 4). Filtering for KEGG Pathways and GO Biological Processes with an adjusted p-value <0.005 showed enrichment for pathways including “Response to IFN-γ” and “Antigen processing and presentation” (Figure 2A, B), which agrees with the increased expression of proteins such as STAT1, WARS1 and components of the antigen processing and presentation machinery (TAP1, TAP2, CD74 and HLA-molecules) (Figure 1D). Pathways reflecting fatty acid metabolism and PPAR signaling were also enriched, being reduced in UCeD crypts (Figure 2A, C). Comparing individual proteins mapped to the pathways displayed in Figure 2 B, C confirmed their increased (Figure 2D) and decreased (Figure 2E) expression in UCeD compared to TCeD and Ctr crypt samples. Strikingly, the expression of key IFN-γ response proteins in UCeD crypts was inversely correlated with expression of proteins involved in cell metabolism, as exemplified by correlations of STAT1-CPT1A, HLA-DRA-HMGCS2 and TAP1-FABP1 (Figure 2F). This observation is suggestive of co-ordinated regulation of these pathways. Moreover, there was a connection in active

CeD between IFN-γ response and tissue remodeling. As part of a previous study, we established histology and proteome scores for the same celiac biopsies (31). Both these scores serve as proxies for tissue remodeling. We observed strong correlations between crypt IFN-γ response and the Vh:Cd ratio and proteome scores (Supplemental Figure 2). Furthermore, the increased expression of proteins reflecting response to IFN-γ was not confined to the crypt region but it was also observed in the villous epithelial cell layer (Supplementary Figure 3).

Upregulation of the antigen presentation pathway in UCeD

IFN-γ is a known inducer of antigen presenting pathway proteins, including MHC class II molecules (32). A study of mice suggested that MHC class II expression on ISCs enables direct interaction of these cells with CD4+ T cells, and ISC subsets found to have differential ability to interact with CD4+ T-cells were defined (33). Relevant to these observations, of three defined ISC subsets (ISC-I, ISC-II and ISC-III) in mice, the crypt proteome data of UCeD was skewed towards the gene-set of the ISC-II subset (Supplemental Figure 4A). Moreover, we observed increased expression of HLA-DRA and HLA-DRB1 in crypts of UCeD vs TCeD and Ctr (Supplemental Figure 4B). To further address expression of MHC class II molecules on gut epithelial cells, we undertook flow cytometry analysis of fresh, non-cryopreserved cells prepared from duodenal biopsies of CeD patients (Supplemental Table 5). Following treatment with EDTA and collagenase, three fractions of cells were obtained from 9 UCeD and 5 TCeD subjects (Supplemental Figure 5A). Staining with antibodies specific for HLA-DR, HLA-DP, HLA-DQ and HLA-DQ2, in EpCAM+ cells (Supplemental Figure 5B-D) we observed cells staining for HLA-DR and HLA-DP with higher signal in UCeD vs TCeD (Figure 3A). No epithelial staining was observed for HLA-DQ, neither in untreated nor treated CeD, whereas CD11c+ cells, as previously demonstrated to be located in the lamina propria (34), stained brightly positive in both conditions (Figure 3B). As could be expected from this result, a negative staining for HLA-DQ was also observed in EpCAM+ cells being CD44+CD117-CD166+CD24- (Supplemental Figure 6) which have been demonstrated to encompass ISCs (35).

Small intestinal remodeling induced by IFN-γ in mice recapitulates key features of CeD

The pathway enrichment analysis points to IFN-γ as the key driver of the crypt proteome changes in UCeD. Because many proteins are shared between cytokine response pathways, we sought to experimentally address whether the observed proteome changes truly reflect IFN-γ mediated processes. Intraperitoneal injection of IFN-γ in mice induces pronounced remodeling in the small intestine with crypt hyperplasia and villous shortening (36, 37). To resolve both time and dose-dependency of the IFN-γ mediated intestinal remodeling processes, we injected mice at 8-hour intervals with 1, 2, 4, 6 or 9 doses of 16.7µg recombinant IFN-γ followed by tissue harvesting 8 hours after the last injection (Figure 4A). A subset of mice was injected with EdU (5-ethynyl-2’-deoxyuridine) 22 hours prior to tissue harvest to determine epithelial cell migration speed. Tissue from the proximal 1/3 of the small intestine was collected, fixed in formalin and paraffin embedded for tissue sectioning. We found that IFN-γ injection resulted in a time and dose dependent increase in dept of proliferating crypt cells as determined by staining for Ki67 with an accompanying reduction in villous height to crypt depth (Vh:Cd) ratio (Figure 4B, C). The IFN-γ induced remodeling also induced a time and dose-dependent increase in epithelial cell turnover rate as determined from measurement of the EdU migration front (Figure 4D, E).

We next sectioned FFPE tissue for isolation of crypt regions by laser capture microdissection and MS-based tissue proteome analysis (n = 63). Following filtering, we identified and quantified 3356 proteins across 52 samples from 28 mice (Supplemental Table 6). PCA revealed a clear dose and time dependent effect of IFN-γ on the crypt proteome expression (Figure 4F). Among the proteomic signals driving PC1 were enzymes involved in carbohydrate and amino acid metabolism, fatty acid metabolism as well as Lyz1 (Supplemental Figure 7A, B). Administration of IFN-γ led to reduction of Lyz1 (Supplemental Figure 7C) indicating a loss of Paneth cells as confirmed by immunofluorescence staining (Supplemental Figure

7D). In UCeD crypts the proteomic signal for Lyz was reduced but not absent (Supplemental Figure 7E). Comparing the fold change of human DEP to fold change of mouse orthologs for mice injected with 9 doses of IFN-γ, we observed clear overlaps in DEP and similar directional changes in protein expression (Figure 4G). Filtering for proteins detected both in human and mouse datasets (n = 1056) and analyzing for enrichment of GO biological processes along PC1, we found overlap in processes such as antigen processing and presentation, and fatty acid metabolism (Supplemental Table 7) (Figure 4H). The expression of proteins mapped to “Antigen processing and presentation” and “Fatty acid beta-oxidation" changed in an IFN-γ dose and time-dependent manner (Figure 4I). In summary, the key remodeling events of CeD with crypt hyperplasia, reduced Vh:Cd ratio and increased epithelial cell turnover occur also in response to IFN-γ injection in mice. In addition, key biological pathways that are altered in the UCeD crypt compartment, including the altered metabolic state with reduced fatty acid metabolism, are also affected by IFN-γ stimulation.

Crypt epithelial IFN-γ signaling is a key driver of tissue remodeling and altered crypt metabolic state

As the IFN-γ receptor is expressed on many cell types, we next sought to determine whether IFN-γ induced remodeling processes reflect indirect effects or direct effects from IFN-γ signaling in the intestinal epithelial compartment. To this end, we generated intestinal epithelial cell specific IFN-γ receptor 1 knock out mice (*Ifngr1*$^{\text{IEC}-/-}$ mice; *Ifngr1*$^{\text{fl/fl}}$ × *Villin*-Cre mice) which together with littermate controls (wild-type, WT) were injected intraperitoneally with 2 or 6 doses of IFN-γ as well as EdU 22 hours prior to euthanasia and analysis (Figure 5A). We found that targeted deletion of *Ifngr1* in the epithelial compartment prevented IFN-γ induced tissue remodeling with reduction in Vh:Cd ratio (Figure 5B). The effect was evident in the crypt compartment (Supplemental Figure 8A) as *Ifngr1*$^{\text{IEC}-/-}$ mice presented with no increase in crypt depth, yet we observed a small, dose dependent IFN-γ induced decrease in villous height (Supplemental Figure 8B). The targeted *Ifngr1* deletion also prevented IFN-γ induced crypt hyperproliferation as determined by EdU incorporation (Figure 5C).

Proteome analysis of laser-capture isolated crypt regions (Supplemental Table 8) revealed a clear separation along PC1 for samples from WT mice injected with IFN-γ which was in contrast to samples from *Ifngr1*$^{\mathrm{IEC-/-}}$ mice receiving no treatment or treated with IFN-γ (Figure 5D). Indeed, proteins mapped to "Antigen processing and presentation" and "Fatty acid beta-oxidation" were altered in IFN-γ treated WT mice (Figure 4 I, Figure 5 E, F), but not in IFN-γ treated *Ifngr1*$^{\mathrm{IEC-/-}}$ mice (Figure 5 E, F). We found that the expression of mouse homologues to proteins from up- or down-regulated biological pathways in UCeD crypts (Figure 2 D, E) increased and decreased respectively upon IFN-γ treatment in WT mice, but not in *Ifngr1*$^{\mathrm{IEC-/-}}$mice (Figure 5 G, H). Similarly, we observed upon IFN-γ treatment a reduced expression of key enzymes involved in the synthesis of ketone bodies (ACAT1, HMGCS2 and BDH1) in WT mice but not in *Ifngr1*$^{\mathrm{IEC-/-}}$mice (Figure 5I). Interestingly, the IFN-γ induced decrease in lipid metabolism was paralleled by an increase in FASN expression which is indicative of increased de novo lipid synthesis (Figure 5J). Protein-protein interaction analysis indicates that proteins from up- or down-regulated biological pathways in UCeD crypts (Figure 2 D, E) form functional networks that reflect intestinal remodeling mediated by IFN-γ through IFN-γR1- and STAT1-signaling (Supplemental Figure 9).

Different kinetics of IFN-γ driven alterations in proteomic signatures

To gain better insight into the link between the crypt response to IFN-γ and the altered cell metabolic profile in the crypt zone, we analyzed proteomic changes in WT mice over the time-course (8h-72h) of 1-9 injections of IFN-γ. One injection of IFN-γ in WT mice was sufficient to induce crypt expression of direct IFN-γ response proteins such as STAT11, WARS and B2M (Figure 6A). Similar kinetics were observed for proteins being involved in the antigen presentation machinery (CD74, TAP1, TAP2, H2-D1, H2-K1) (Figure 6A). Proteins reflecting ketone body synthesis, fatty acid beta-oxidation and retinoid metabolism (Figure 6B) decreased in a dose and time dependent manner, but generally with more protracted kinetics. FASN, indicative of de novo lipid synthesis, increased already following one injection of IFN-γ (Figure 6C). Overall, these data point to a coordinated response to IFN-γ both involving antigen presentation machinery and cell metabolic changes.

Discussion

By using spatial tissue-proteomics we demonstrate that IFN-γ is a driver of crypt hyperplasia in CeD by acting directly on crypt epithelial cells. The changes are strikingly paralleled by changes in cell metabolism which suggests that epithelial cell proliferation and hyperplasia are linked with metabolic changes. The implications of the findings go beyond CeD as crypt hyperplasia is observed in many inflammatory conditions of the small intestine, like tropical sprue, bacterial overgrowth syndrome, autoimmune enteropathy and graft-vs-host disease (2).

Our findings place T cells via the production of IFN-γ as the driver of crypt hyperplasia by action on epithelial cells in the crypt region. The T cells involved could be CD4+ T cells in the lamina propria, or intraepithelial CD8+ T cells as both cell types produce IFN-γ. In the active CeD lesion intraepithelial CD8+ T cells seem to produce more IFN-γ than lamina propria CD4+ T cells (16, 17). Notwithstanding, as the gluten-specific CD4+ T cells in CeD are located in lamina propria spatially close to the crypts (11, 38) and intraepithelial CD8+ cells typically accumulate at the villous tip distant to the crypt zone (39) the gluten-specific CD4+ T cells may be particularly important for mediating IFN-γ effects on crypt epithelial cells in CeD.

The IFN-γ induced signature in crypt epithelial cells includes a program for “Antigen presentation” with upregulated expression of invariant chain (CD74) and MHC class II molecules. This signature points to a role of epithelial cells in antigen presentation to CD4+ T cells. In fact, in mouse models it was demonstrated that ISCs are involved in antigen presentation to CD4+ T cells (33), and further that intestinal epithelial cells in organoid cultures can present gluten antigen (40). Staining of fresh epithelial cells prepared from duodenal biopsies of CeD patients confirmed the epithelial cell expression of MHC class II molecules (both HLA-DR and HLA-DP), and we observed an increased expression in untreated patients compared to patients in remission. This finding indeed suggests an antigen presenting role of epithelial cells for CD4+ T cells. We were particularly interested in addressing whether epithelial cells, and especially ISCs, can be involved as antigen presenting cells in the IFN-γ controlled circuit that gives crypt hyperplasia in CeD. Importantly, only disease-associated HLA-DQ allotypes are involved in presentation of gluten peptides to CD4+ T cells in CeD (10). In contrast to a prior study (40), but in accordance with several other studies (38, 41-43), we observed no expression of HLA-DQ by epithelial (EpCAM+) cells, including CD44+CD117-CD166+CD24- cells that should encompass ISCs (35). Epithelial cells in culture on stimulation by IFN-γ show differential expression of MHC II isotypes, and with a higher concentration of IFN-γ needed for the expression of HLA-DQ (44, 45). This fact likely explains the absence of duodenal epithelial HLA-DQ expression in CeD. Based on these findings we conclude that within the gut mucosa of the CeD lesion there are other antigen presenting cell than epithelial cells, like HLA-DQ expressing CD11c+ dendritic cells (34) or possibly plasma cells (46), that present antigen to gluten-specific CD4+ T cells.

Guy-Grand et al. demonstrated that systemic administration of IFN-γ in mice leads to crypt cell hyperplasia, villous shortening and increased crypt area suggestive of increased cell divisions (36). These changes did not require presence of intraepithelial lymphocytes as the changes were also observed in mouse strains lacking intraepithelial lymphocytes, including germ-free mice, common cytokine receptor γ-chain mutant mice and RAG-2/γ-chain double mutant mice. Interestingly, the non-requirement of intraepithelial lymphocytes for the effects of IFN-γ contrasted with the changes induced by interleukin-12 (IL-12). While systemic administration of IL-12 led to increased epithelial cell turnover and also villous epithelial damage, these effects necessitated the presence of intraepithelial lymphocytes. Eriguchi et al. on administering mice IFN-γ also observed small intestinal crypt hyperplasia and villous shortening, as well as change of ISC phenotypic markers (37). Takashima and coworkers studying intestinal graft versus host disease, a condition characterized by crypt cell hyperplasia with increase of proliferating Ki67+ cells, observed increased death of ISCs being mediated by IFN-γ (47). They later reported that these graft versus host manifestations, including crypt cell proliferation, involve STAT1 and the IFN-γ receptor of gut epithelial cells, and further that low doses of IFN-γ induce cell divisions in epithelial only organoid cultures (48). Omrani et al. studying age related changes in the gut, concluded that by older age there is increased production of IFN-γ by T cells in the lamina propria and that IFN-γ acting on crypt cells gives ISC activation and exit from a stem state towards cells that express MHC II genes which are proliferating and transcriptionally primed towards the secretory lineage (49). In addition, the authors observed a reduction of ISCs in older mice. In gut biopsies of CeD patients in remission who have been orally challenged with gluten there is an increased goblet cell signature (50, 51) - observations which are in line with a disease-related bias of ISCs toward secretory fate. Papers addressing the effect of IFN-γ on Paneth cells have reported that IFN-γ induces apoptosis of these cells (37, 52, 53), and also that IFN-γ is a trigger for Paneth cell degranulation and extrusion (53). We also found effects of IFN-γ on Paneth cells in mice with reduced lysosome expression on prolonged injection of the cytokine. Studies of CeD have reported diminished or normal numbers of Paneth cells in the active lesion (54-56), less lysozyme activity in CeD jejunal tissue (54) and also that the cells have reduced content of lysozyme (55). Our proteomic data are in agreement with these findings as we found less lysozyme protein expression in crypt regions of active CeD patients versus controls. Thus, in essence IFN-γ induces a loss of ISCs, but at the same time the cytokine instigates a program that results in increased cell proliferation in the transit amplifying zone thereby giving crypt hyperplasia and increased epithelial cell turnover. Taken together, the findings of the literature align well with our notion that crypt hyperplasia in celiac disease is mainly caused by a direct effect of IFN-γ on crypt epithelial cells.

In mice dietary interventions have been demonstrated to affect expression of HMGCS2 and CPT1A in ISCs (57, 58). A high glucose diet was shown to induce a diminished expression of HMGCS2 (57) similar to what we observe in the crypt zones of untreated CeD and of mice treated with IFN-γ. Gebert et al.

analyzing proteome changes in intestinal crypts on aging in mice observed both increased expression of MHC class II and CD74 and interestingly also a reduced expression of HMGCS2 (59). This observation suggests that the induced IFN-γ immune signature and the metabolic changes with reduced expression of key metabolic enzymes are causally related. Further, similarly to what has been reported for IFN-γ treated mice, an impaired function and a reduced number of ISCs was observed in mice with a genetic ablation of *Hmgcs2* in Lgr5+ ISCs (57). Given this scenario, it seems likely that the damage of ISCs being induced by IFN-γ is mediated by the changes in crypt cell metabolism. Changes in crypt cell metabolism could also be involved in the IFN-γ induced bias towards the secretory linage as well as the increased proliferation of cells causing crypt hyperplasia. Relevant to these considerations is the observation that a high fat diet in mice lead to decreased epithelial expression of MHC class II molecules which mechanistically was proven to be mediated by less IFN-γ being produced due to a reduced intestinal microbiome diversity (60). It remains a possibility that the effects of high glucose diet on the crypt cell metabolism could be mediated at least in part by an immune reaction to an altered microbiota with more production of IFN-γ.

While our results align with the model proposed by MacDonald et al. (28, 29) in that the primary driver of crypt hyperplasia is at the level of ISCs, it differs from this model in that the effect of T cells is mediated directly by IFN-γ on and not indirectly via lamina propria fibroblasts by production of keratinocyte growth factor. The results should, however, not be taken to imply that lamina propria fibroblasts, which consists of several subtypes (61), are not involved in the pathogenesis of CeD. There are several candidate pathways for involvement. Intestinal fibroblasts are critical for formation of the intestinal stem cell niche by providing structural support and producing several factors of importance for ISCs differentiation (62), such cells produce IL-6 which is important for plasma cell survival (63), and as recently demonstrated using an organoid model, fibroblasts produce the B-cell and T-cell growth factor IL-7 after stimulation by activated gluten-specific CD4+ T cells (64).

Our findings indicate that increased cells division in the transit amplifying zone, resulting in crypt hyperplasia and increased cell turnover is part of an active program instigated at the stem cell zone, rather than solely a mechanism to compensate for loss of epithelial cells killed toward the villous tip. The results give support to a model of crypt hyperplasia as a consequence of increased crypt cell division following T-cell activation, yet the effect is caused by a direct action of IFN-γ on crypt epithelial cells, not an indirect action involving stromal fibroblasts. As crypt hyperplasia, increased epithelial cell turnover and villous blunting are observed in many inflammatory conditions of the small intestine, likely these changes are integral parts of a defense program operating in conditions where IFN-γ is the central inflammatory mediator.

Materials and methods

Sex as a biological variant. Duodenal biopsies from both female and male adult human subjects were used for spatial proteomics analysis and flow cytometry analysis. Experiments on mice with repeat injection of IFN-γ were done using female C57BL/6 mice. Experiments on mice with targeted deletion of *Ifngr1* was performed on littermates which were both female and male. The findings are expected to be relevant to both males and females, although no experiments were performed to test for sex-related differences.

Human subjects. For spatial proteomics analysis we used archival formalin fixed paraffin embedded (FFPE) duodenal biopsy material from adults that underwent gastroduodenoscopy at Oslo University Hospital-Rikshospitalet between 2012-2023. The patient cohort has previously been described (31), in addition to 4 subjects that were not included in the previous study (2 CeD and 2 Ctr). In total we analyzed FFPE tissue sections from 20 adults with biopsy-proven CeD, comparing biopsies collected at the time of diagnosis (untreated CeD; UCeD, Marsh 3) to biopsies collected at follow-up after treatment with gluten free diet (Treated CeD; TCeD, Marsh 0). As disease controls, we analyzed biopsies from 20 non-CeD adults with normal duodenal histology (Marsh 0) (Supplemental Table 1). For flow cytometry analysis of gut epithelial cell MHC II expression, we analyzed biopsies from 9 UCeD patients and 5 TCeD patients who visited the endoscopy unit at Oslo University Hospital–Rikshospitalet for diagnostic examination and clinical follow-up of CeD (Supplemental Table 5). The diagnosis of CeD was made according to established guidelines (21).

Mouse experiments. C57BL/6J mice (female; age 9-11 weeks; Janvier Lab) were injected intraperitoneally with recombinant IFN-γ (GenScript, Z02916-1) dissolved in sterile dPBS. Single doses of 16.7 µg IFN-γ in 200 µl sterile PBS were injected at 8-hour intervals followed by euthanasia 8 hours after the last injection. Four independent experiments were performed on 28 mice that were either treated with PBS (n = 6) or IFN-γ; 1 dose (n = 4), 2 doses (n = 4), 4 doses (n = 4), 6 doses (n = 4) and 9 doses (n = 6). In two of the experiments, mice were also injected with intraperitoneally with 100 µl of 0.1 mg EdU in 10% DMSO / PBS) 22 hours prior to euthanasia.

To generate mice with targeted deletion of *Ifngr1* in the epithelial cell compartment, *Ifngr1*flox/flox mice (stock #025394, Jackson Laboratory) (65) were crossed with heterozygous villin-cre (vil1-cre) transgenic mice (stock #021504, Jackson Laboratory) (66), both on C57BL/6 background. From the filial (F) 1 progeny, *Ifngr1* flox/wt Vil1-cre transgenic mice were bred to *Ifngr1* flox/flox mice to generate *Ifngr1* flox/flox Vil1-cre transgenic *Ifngr1*$^{IEC-/-}$ mice. Vil1-cre negative littermates with wild-type (WT) expression of *Ifngr1* in epithelial cells were used as control (WT) mice for IFN-γ injection experiments. Mice (9-11 weeks) with targeted deletion of *Ifngr1* (n = 9) or Vil1-cre negative littermate controls (n = 6) were untreated (n = 4) (CTR) or treated with 2 doses (n = 6) or 6 doses (n = 5) of IFN-γ as well as EdU injection 22 hrs prior to euthanasia.

Mice were euthanized by cervical dislocation 8 hours after the last injection with IFN-γ. The small intestine was quickly harvested and flushed with ice-cold PBS. From all mice the proximal 1/3 of the small intestine was collected and fixed in Neutral Buffered Formalin in the dark over night at room temperature. From 4 mice (PBS n = 2; IFN9 n = 2), also the middle (2/3) and distal (3/3) part of the small intestine was collected. After fixation, 4-7 pieces of ~4-5 mm were cut tangentially and oriented in Tissue-Tek 2-lane paraform gels (Sakura, USA) for paraffin embedding.

Tissue sectioning and laser capture microdissection

Human samples. For human duodenal biopsies, eight µm FFPE tissue sections were adhered to UV-treated PEN-covered slides (Zeiss). Sections were dewaxed in xylene (x2) hydrated in 100 % ethanol, 95 % ethanol and 70 % ethanol (1 min each) followed by 2 x 1 min in water. Sections were stained with

Mayer's hematoxylin solution ~30 s, rinsed in tap water, incubated in hexamine (1 min) followed by 1min in water and 30 s in Azophoxine solution, rinsing in water and airdried. For mouse intestinal sections, five µm FFPE paraffin block sections were adhered to UV-treated PEN-covered slides (Zeiss) followed by staining with hematoxylin as previously described (50). Sections were stored in dehydrator boxes and dried at 37°C prior to laser capture microdissection. Crypt regions were isolated using a PALM MicroBeam laser capture microdissection system (Carl Zeiss MicroImaging, Munich, Germany) capturing tissue into 0.5ml opaque adhesive cap tubes (Zeiss). Crypt regions that encompass intestinal stem cells, Paneth cells as well as 4-5 daughter cells were isolated. In sections from human biopsies, well oriented crypts were identified based on visual presence of Azophoxine stained Paneth cells. Two replicate samples were collected for most biopsies (~150 000 µm^2 per sample) (n = 109).

Mouse samples. Five µm tissue sections from FFPE embedded mouse intestine were adhered to UV-treated PEN-covered slides (Zeiss), dewaxed as described above and stained with Mayer's hematoxylin solution. Crypt regions were isolated using a PALM MicroBeam laser capture microdissection system (Carl Zeiss MicroImaging, Munich, Germany) capturing tissue into 0.5 ml opaque adhesive cap tubes (Zeiss). Crypt regions that encompass intestinal stem cells, Paneth cells as well as 4-5 daughter cells were isolated based on visual assessment of tissue orientation in intestinal cross-sections. Crypt regions were isolated from the proximal part of the small intestine unless otherwise specified. For each sample, crypts were isolated and pooled from all embedded tissue pieces, collecting 1-3 replicate samples per tissue block (n = 63 samples from n = 28 mice). From 4 mice, also crypts from the middle and distal intestine were collected and processed for MS analysis.

Sample processing, LC–MS/MS (TimsTOF) and raw data analysis

Laser capture microdissection isolated samples were processed as previously described (50). Dissected tissue was retrieved from adhesive caps using ammonium bicarbonate (10 µl 50 mM) with ProteaseMax Surfactant (0.2 %) followed by ammonium bicarbonate (10 µl 50 mM) and transferred to

0.5 ml LoBind tubes (Eppendorf, Hamburg, Germany). Samples were heated to 98°C for 90 min followed by sonication in water bath for 60 min. Disulfide bridges were reduced by addition of dithiotreitol (2 µl 0.1 M) followed by incubation for 20 min at 56°C and alkylated by addition of iodoacetamide (2 µl 55 mM) followed by incubation for 15 min in the dark at room temperature. Samples were digested by addition of trypsin (1.5 µl 10 µg/g) and incubated over night at 37°C. Peptides were purified by solid-phase extraction either by using stage tips with 3 layers of C18 Empore Extraction Disks or C18 micro columns or loaded on EvoTips according to the manufacturer's instruction.

Crypt samples (n = 109) from human biopsies were analyzed using an EVOSEP liquid chromatography system connected to a quadrupole – Orbitrap (QExactive HF) mass spectrometer (ThermoElectron, Bremen, Germany) equipped with a nanoelectrospray ion source (EasySpray/Thermo). For liquid chromatography separation we used a 15 cm C18 column (Column details: 15 µm beads, 150 µm inner diameter, 15 cm long, EV-1074). The standard EVOSEP method 30 samples/day was used. The mass spectrometer was operated in the data-dependent mode to automatically switch between MS and MS/MS acquisition. Survey full scan MS spectra (from m/z 375 to 1,500) were acquired in the Orbitrap with resolution R = 60,000 at m/z 200 (after accumulation to a target of 3,000,000 ions in the quadruple). The method used allowed sequential isolation of the most intense multiple-charged ions, up to seven, depending on signal intensity, for fragmentation on the HCD cell using high-energy collision dissociation at a target value of 100,000 charges or maximum acquisition time of 110 ms. MS/MS scans were collected at 60,000 resolution at the Orbitrap cell. Target ions already selected for MS/MS were dynamically excluded for 30 seconds. General mass spectrometry conditions were: electrospray voltage, 2.0 kV; no sheath and auxiliary gas flow, heated capillary temperature of 250°C, normalized HCD collision energy 28 %.

Crypt samples from mice injected with IFN-γ and controls (n = 63) were processed and analyzed by ultra-high-performance LC (UHPLC) and trapped ion mobility spectrometry (tims) time-of-flight (TOF)

MS. Digested peptides were cleaned by solid-phase extraction using stage tips with 3 layers of C18 Empore Extraction Disks, vacuum dried and redissolved in 0.1% FA before injected to a nanoElute UHPLC coupled to a timsTOFfleX or a timsTOFPro2 mass spectrometer via a CaptiveSpray ion source (Bruker Daltonics, Bremen, Germany). For liquid chromatography separation we used a 25cm C18 column (Column details: 1.6-µm beads, 120 Å pore size, 75-µm inner diameter, 25 cm long, Aurora UHPLC column, IonOptics) with a flow rate of 0.3 µl/min. Solvent A (0.1% FA) and solvent B (acetonitrile in 0.1% FA) were used for a gradient of 0% to 35% solvent B in 60 minutes. Crypt samples from C57Bl/6J mice injected with IFN-γ were ran as four independent experiments on timsTOF-fleX operated in data-dependent parallel (DDA) accumulation-serial fragmentation (PASEF) mode, recording mass spectra for MS and tandem MS (MS/MS) scans between 100 and 1700 m/z. The ion mobility resolution was 0.60 to 1.60 V s cm−2 over a 100-ms ramp time. Ten PASEF MS/MS scans per cycle with a nearly 100% duty cycle were used for data-dependent acquisition. We applied a polygon filter in the m/z and ion mobility space to exclude low m/z singly charged ions from the PASEF precursor selection and applied an active exclusion time of 0.4 minutes to precursors that reached 20,000 intensity units. Collisional energy was ramped stepwise as a function of ion mobility.

Crypt samples from *Ifngr1*$^{IEC-/-}$ mice and littermate controls (n = 15) were analyzed on a timsTOFPro2 instrument operating in data independent acquisition (DIA) PASEF mode. Mass spectra for MS were recorded between m/z 100 and 1700. Ion mobility resolution was set to 0.85–1.30 V·s/cm over a ramp time of 100 ms. The MS/MS mass range was limited to m/z 475-1000 and ion mobility resolution to 0.85-1.30 V s/cm to exclude singly changed ions. The estimated cycle time was 0.95 s with 8 cycles using DIA windows of 25 Da. Collisional energy was ramped from 20eV at 0.60 V s/cm to 59eV at 1.60 V s/cm

Protein identification and data processing

Data from human samples. MS raw files from human crypt samples (.raw files) (n = 109) were processed in the MaxQuant environment (67) (version 1.6.1.0) with the integrated Andromeda search engine for peptide and protein identification, with an FDR threshold of 0.01 for peptide and for protein identification. The human UniProtKB FASTA database (September 2018; 20394 entries) was used as forward database for protein identification. Match between runs was enabled and label-free protein quantification (LFQ) was performed using the MaxQuant's Label Free Quantification algorithm with a minimum ratio count of one. Methionine oxidation and N-terminal acetylation was used as variable modification and carbamidomethyl cysteine as fixed modification. Processing of MS raw files from LCM isolated villous epithelium (n = 16 samples isolated from n = 3 UCeD, n = 2 TCeD and n = 2 Ctr biopsies) has previously been described (68).

The ProteinGroups.txt output was processed in Perseus (version 1.6.15.0) (69). For all datasets, proteins matched to the reverse decoy database, identified by site or identified as potential contaminant were removed. LFQ expression data were log2 transformed. Data was filtered to keep only proteins with valid LFQ-values in at least 70% of the samples in at least one of sample-groups (UCeD, TCeD or Ctr) resulting in 1333 protein groups of which 1329 were annotated to gene name. Missing values were imputed for each sample based on normal distribution to simulate low abundant LFQ values and replicate samples from the same biopsy tissue block were averaged prior to statistical analysis. Data were z-scored per row using median value. Biological pathways were annotated to proteins in Perseus, selecting GO Biological Processes, GO Molecular Function, GO Cellular Component and KEGG.

Data from mouse samples. MS raw files (.d) files from mouse crypt samples (n = 63) analyzed by DDA-PASEF MS were processed with MSFragger (version 4.1) (70, 71) via FragPipe (version 22.0) using the mouse UniProtKB FASTA database (January 2019, 17006 entries) as forward database. Methionine oxidation and N-terminal acetylation was used as variable modification and carbamidomethyl cysteine as fixed modification. Proteins were quantified by MaxLFQ using IonQuant. MS raw files (.d) files from mouse crypt samples analyzed by DIA-PASEF MS (n = 15) were processed with MSFragger (version 4.1) calling DiaNN via FragPipe (version 22.0) using the default parameters of the DIA SpecLib_Quant_diaPASEF workflow with MaxLFQ quantification of proteins.

The report.pg.matrix.tsv outputs were processed in Perseus (version 1.6.15.0) (69), and proteins identified as potential contaminants were removed. LFQ expression data were log2 transformed. Data was filtered to keep only proteins with valid LFQ-values in at least 70% of the samples in at least one of sample-groups resulting in 3371 protein groups annotated to 3356 genes. Missing values were imputed for each sample based on normal distribution to simulate low abundant LFQ values. For the DDA dataset (n = 63) batch effect correction was performed in Perseus via the R plugin using the limma package (72). Only samples from proximal small intestine (n = 52) were included for downstream data analysis.

For the DIA dataset (n = 15), samples with valid LFQ values lower than the median minus two times the standard deviation across all runs were excluded from downstream analysis (n = 3). Data was filtered to keep only proteins with valid LFQ-values 70 % across all samples resulting in 6653 protein groups annotated to 6594 genes across n = 12 samples. Biological pathways were annotated to proteins in Perseus, selecting Gene Ontology (GO) Biological Processes, GO Molecular Function, GO Cellular Component and KEGG.

Proteomics data analysis and visualization

Global protein expression was compared between sample groups using unpaired two-sided Student's *t* test with permutation-based FDR control (FDR< 0.05; 250 randomizations). A *P* value lower than 0.01

was considered significant. Biological pathway annotation of proteins was exported from Perseus and expression of proteins mapped to biological pathways were compared between groups by Mann Whitney U with Benjamini-Hochberg correction for multiple testing. All boxplots show the median (center line) with interquartile range (25 % to 75 %) and whiskers show the furthest point within the 1.5x interquartile length. Pathway enrichment analysis was performed by enabling categorical enrichment during principal component analysis in Perseus (Benjamin-Hochberg controlled FDR < 0.05). The resulting categories (enriched pathways), difference and adjusted p-values were exported and proteins from the crypt datasets were mapped to the pathways. To compare mouse and human data, human gene names were converted to mouse gene orthologs using the "homologene" package in R followed by manual annotation of missing genes. To estimate time and IFN-γ dose-dependent change in protein expression locally weighted regression (LOESS) smoothing was applied using the loess() function in R within the ggplot2 package. Default parameters were used, including a smoothing span of 0.75 and a polynomial degree of 2. Confidence intervals were estimated using standard errors derived from LOESS smoothing. The model was applied independently to each protein analyzed. As measure of kinetics, we calculated the point of the curve at 50% change in expression comparing 0 and 9 IFN-γ injections. For human crypt proteome data, median z-scored expression of proteins mapped to the GO Biological Pathway "Response to interferon gamma" was calculated for each biopsy and correlated to published Vh:Cd ratio and biopsy proteome scores (Pearson's correlation). Proteins from up or downregulated biological processes in human crypts were subjected to protein-protein interaction networks analysis using StringDB (73). Each node represents a protein, and each edge represents a physical or functional interaction between proteins. Networks were exported to Cytoscape 3.10.1 (74) and overlayed with Student's t-test log2 difference from human crypts (UCeD vs Ctr) and mouse crypts (IFNx9 vs PBS) to annotate node size and node fill respectively. Mouse orthologs for HLA molecules were manually assigned. Nodes were manually assigned to functional groups shown as gray regions. Data was plotted in R (v 4.2.3) using R Studio (build 421) using the ggplot2 package, and the final figures were assembled from pdf files in Adobe Illustrator.

Immunofluorescence staining and detection of EdU in mouse small intestine

Three µm FFPE sections were deparaffinized and subjected to heat induced antigen retrieval using high pH antigen retrieval by incubation preheated buffer in a water bath at 98°C for 20 min followed by cooling for 20 min at room temperature. Sections were stained with monoclonal rabbit-anti-Ki67 (clone SP6 from Dako or Abcam) or rabbit-anti-lysozyme (Dako, EC 3.2.1.17) followed by detection with goat-anti-rabbit-A488 (Molecular Probes, A-11034) or donkey-anti-rabbit-Cy3 (Jackson ImmunoResearch, 711-165-152). Incorporated EdU was detected using the Click-iT™ EdU Cell Proliferation Kit for Imaging (Invitrogen) according to the manufacturer's instructions. Slides were counterstained with 40,6-diamidino-2-phenylindole (DAPI) and mounted with ProLong Diamond Antifade Mountant (ThermoFisher). Slides were imaged at room temperature on an inverted Nikon fluorescence microscope (Nikon Eclipse Ti-S; Nikon, Tokyo, Japan) using a Nikon 9 10/0.3 or 9 20/0.45 Plan Fluor lens (Nikon) and NIS ELEMENTS BR 5.30.04 software (Nikon). Images were processed in Fiji/ImageJ (2.9.0/1.53t) (75).

Measurement of villous height to crypt depth ratio and EdU migration front.

Measurement of villous height (Vh) to crypt depth (Cd) ratios (Vh:Cd) was performed on immunofluorescent images stained for DAPI and Ki67. Crypt depth was measured from the crypt bottom to the end of Ki67 signal. Villous height was measured from the end of Ki67 signal to the tip of the villous as defined by DAPI signal. From each mouse, 3-5 segments from the proximal part of the intestine were analyzed (3-6 villous-crypt pairs per segment). Average values for each mouse are reported. EdU migration front was measured on immunofluorescence images stained for DAPI and EdU, measuring from the crypt bottom to the end of EdU signal and reported in µm. Migration speed was calculated by dividing distance from the migration front to crypt bottom (µm) on time since EdU injection (22 hours). Values represent mean values for 5-7 segments (3-5 crypts per segment) for each mouse. For C57Bl/6J mice injected with 9 doses IFN-γ and for *Ifngr1*$^{IEC-/-}$ littermate control mice injected with 6 doses IFN-γ, the EdU migration front had reached the end of the villi and the calculated migration speed therefore represent the minimum migration velocity.

Flow cytometry analysis of MHC II expression on gut epithelial cells

Biopsy specimens from the duodenum were collected from adult subjects. Each subject donated 4 to 12 duodenal biopsy samples. The biopsy specimens were placed in ice-cold RPMI-1640 immediately after collection. The biopsies were treated twice with 2 mM EDTA in 2% FCS in PBS for 10 min at 37°C to release the intestinal epithelial cell layer. Subsequently, the biopsies were finely chopped with surgical scissors and subjected to two rounds of digestion with 1 mg/ml collagenase type 4 (Worthington Biochemical) in 2 % FCS in HBSS at 37°C for 45 min. During both the EDTA treatment and the pooled collagenase digestions, the samples were placed on rotation to ensure consistent exposure of the tissue to the reagents. After the first round of collagenase digestion, the samples were further homogenized using a 1 ml pipette and filtered through a 40 µm cell strainer to obtain a suspension of lamina propria cells. Remaining undigested pieces were treated with buffer containing fresh collagenase for a second round of digestion. Single cell suspensions of the two EDTA fractions and the pooled fractions from collagenase treatment were subsequently used for flow cytometry analysis. We used a 24-color antibody panel (Supplemental Table 9) to stain the tissue samples for 30 min on ice with a mix of antibodies including a LIVE/DEAD marker. This panel included the monoclonal antibodies SPV-L3 (anti-HLA-DQ pan) and 2.12.E11 (anti-HLA-DQ2) which on HLA-DQ2 molecules recognize non-overlapping epitopes (76). The samples of the three single cell suspension fractions were analyzed on a SONY ID7000 spectral flow cytometer at the Flow Cytometry Core Facility at Oslo University Hospital. Autofluorescence correction is a unique feature in spectral flow cytometry and was applied to all acquired samples. Fluorescence minus one (FMO) controls for the HLA-DQ reactive antibodies were undertaken for all three cell fractions. The flow cytometry data was analyzed with FlowJo software version 10.10.0.

Statistics. Statistical analysis was performed in Persues or in R (version 4.2.3) using R Studio (build 421). The details of statistical analysis, including n, test used, significance and correction for multiple hypothesis testing are described in the Material and methods and/or reported in the figure legends. All presented boxplots show the median (center line) with interquartile range (25 % to 75 %) and whiskers show the furthest point within the 1.5x interquartile length.

Study approval. All subjects had given written informed consent to donate material to research prior to participation. The gut biopsies were part of the institutional research biobank (#20521), and the use of the material was approved by the Norwegian Regional Committee for Medical and Health Research Ethics South-East (REK Sør-Øst; Approval #6544).

All mouse experiments were approved by the Norwegian Food Safety Authority (Mattilsynet) (FOTS 22198, 30621).

Data availability. Mass spectrometry proteomics data have been deposited to the ProteomeXchange Consortium via the PRIDE (77) partner repository with the dataset identifiers PXD062610 and PXD062684**.** Data from the study can be found in the Supplemental Material, Supplemental Tables and values for datapoints in Figure graphs are reported in the "Supporting data values".xls file. Any additional information required to reanalyze the data reported in this paper is available from the corresponding authors upon request.

Author contributions

JS designed the research, performed tissue proteomic experiments, immunofluorescence experiments, analyzed the data, and wrote the manuscript. DS performed tissue proteomic experiments and data analysis on human samples. MfDP and AD designed and performed mouse experiments. LFR designed and analyzed flow cytometry experiments on human gut biopsies. JaS performed flow cytometry experiments. MS performed proteomic analysis. KEAL was responsible for biobanking of human samples. LMS designed the research, wrote the manuscript, and supervised the project. All authors approved the final manuscript.

Acknowledgements. The authors thank the patients who donated biological material, and the staff at the Endoscopy Unit, Oslo University Hospital – Rikshospitalet for collecting this material. The authors are also grateful to Kjersti T. Hagen for preparation of FFPE tissue sections, Anette Johansen for help with sample processing, Liv Kleppa for help with mouse experimental work, the staff of the Department of Comparative Medicine, Oslo University Hospital - Rikshospitalet for animal husbandry and the staff at the Section of Transplantation Immunology, Department of Immunology, Oslo University Hospital - Rikshospitalet for HLA typing.

Funding. This work was supported by a grant from Stiftelsen Kristian Gerhard Jebsen (project SKGJ-MED-017) and the Research Council of Norway (projects 295844 and 324302). The PALM Microbeam is part of the Advanced Imaging Core Facility and proteomics analysis was performed at the Proteomics Core Facility, both supported by the Core Facilities program of the South-Eastern Norway Regional Health Authority. The Proteomics Core Facility is a member of the National Network of Advanced Proteomics Infrastructure (NAPI) that is funded by the Research Council of Norway INFRASTRUKTUR-program (project 295910).

References

1. Savidge TC, Shmakov AN, Walker-Smith JA, and Phillips AD. Epithelial cell proliferation in childhood enteropathies. *Gut.* 1996;39(2):185-93.
2. Robert ME. In: Odze RD, and Goldblum JR eds. *Surgical pathology of the GI tract, liver, biliary tract and pancreas*. Philadelphia: Elsevier; 2009:321-54.
3. Barker N, van Es JH, Kuipers J, Kujala P, van den Born M, Cozijnsen M, et al. Identification of stem cells in small intestine and colon by marker gene Lgr5. *Nature.* 2007;449(7165):1003-7.
4. Lipkin M, Sherlock P, and Bell B. Cell proliferation kinetics in the gastrointestinal tract of man. Ii. Cell renewal in stomach, ileum, colon, and rectum. *Gastroenterology.* 1963;45:721-9.
5. Macdonald WC, Trier JS, and Everett NB. Cell proliferation and migration in the stomach, duodenum, and rectum of man: Radioautographic studies. *Gastroenterology.* 1964;46:405-17.
6. Catassi C, Verdu EF, Bai JC, and Lionetti E. Coeliac disease. *Lancet.* 2022;399(10344):2413-26.
7. Shiner M, and Doniach I. Histopathologic studies in steatorrhea. *Gastroenterology.* 1960;38:419-40.
8. Wright N, Watson A, Morley A, Appleton D, and Marks J. Cell kinetics in flat (avillous) mucosa of the human small intestine. *Gut.* 1973;14(9):701-10.
9. Savidge TC, Walker-Smith JA, Phillips AD, and Savidge TC. Intestinal proliferation in coeliac disease: looking into the crypt. *Gut.* 1995;36(3):321-3.
10. Iversen R, and Sollid LM. The immunobiology and pathogenesis of celiac disease. *Annu Rev Pathol.* 2023;18:47-70.
11. Lundin KEA, Scott H, Hansen T, Paulsen G, Halstensen TS, Fausa O, et al. Gliadin-specific, HLA-DQ(α1*0501,β1*0201) restricted T cells isolated from the small intestinal mucosa of celiac disease patients. *J Exp Med.* 1993;178(1):187-96.
12. Mayassi T, and Jabri B. Human intraepithelial lymphocytes. *Mucosal Immunol.* 2018;11(5):1281-9.
13. Christophersen A, Lund EG, Snir O, Sola E, Kanduri C, Dahal-Koirala S, et al. Distinct phenotype of CD4$^+$ T cells driving celiac disease identified in multiple autoimmune conditions. *Nat Med.* 2019;25(5):734-7.
14. Nilsen EM, Lundin KE, Krajci P, Scott H, Sollid LM, and Brandtzaeg P. Gluten specific, HLA-DQ restricted T cells from coeliac mucosa produce cytokines with Th1 or Th0 profile dominated by interferon gamma. *Gut.* 1995;37(6):766-76.
15. Nilsen EM, Jahnsen FL, Lundin KE, Johansen FE, Fausa O, Sollid LM, et al. Gluten induces an intestinal cytokine response strongly dominated by interferon γ in patients with celiac disease. *Gastroenterology.* 1998;115(3):551-63.
16. Olaussen RW, Johansen FE, Lundin KE, Jahnsen J, Brandtzaeg P, and Farstad IN. Interferon-γ-secreting T cells localize to the epithelium in coeliac disease. *Scand J Immunol.* 2002;56(6):652-64.
17. Forsberg G, Hernell O, Melgar S, Israelsson A, Hammarstrom S, and Hammarstrom ML. Paradoxical coexpression of proinflammatory and down-regulatory cytokines in intestinal T cells in childhood celiac disease. *Gastroenterology.* 2002;123(3):667-78.
18. Tutturen AEV, Dorum S, Clancy T, Reims HM, Christophersen A, Lundin KEA, et al. Characterization of the small intestinal lesion in celiac disease by label-free quantitative mass spectrometry. *Am J Pathol.* 2018;188(7):1563-79.
19. Dotsenko V, Tewes B, Hils M, Pasternack R, Isola J, Taavela J, et al. Transcriptomic analysis of intestine following administration of a transglutaminase 2 inhibitor to prevent gluten-induced intestinal damage in celiac disease. *Nat Immunol.* 2024;25(7):1218-30.
20. Oberhuber G, Granditsch G, and Vogelsang H. The histopathology of coeliac disease: time for a standardized report scheme for pathologists. *Eur J Gastroenterol Hepatol.* 1999;11(10):1185-94.

21. Al-Toma A, Volta U, Auricchio R, Castillejo G, Sanders DS, Cellier C, et al. European Society for the Study of Coeliac Disease (ESsCD) guideline for coeliac disease and other gluten-related disorders. *United European Gastroenterol J.* 2019;7(5):583-613.
22. Meresse B, Chen Z, Ciszewski C, Tretiakova M, Bhagat G, Krausz TN, et al. Coordinated induction by IL15 of a TCR-independent NKG2D signaling pathway converts CTL into lymphokine-activated killer cells in celiac disease. *Immunity.* 2004;21(3):357-66.
23. Hue S, Mention JJ, Monteiro RC, Zhang S, Cellier C, Schmitz J, et al. A direct role for NKG2D/MICA interaction in villous atrophy during celiac disease. *Immunity.* 2004;21(3):367-77.
24. Mayassi T, Ladell K, Gudjonson H, McLaren JE, Shaw DG, Tran MT, et al. Chronic inflammation permanently reshapes tissue-resident immunity in celiac disease. *Cell.* 2019;176(5):967-81 e19.
25. Abadie V, Han AS, Jabri B, and Sollid LM. New insights on genes, gluten, and immunopathogenesis of celiac disease. *Gastroenterology.* 2024;167(1):4-22.
26. MacDonald TT, and Spencer J. Evidence that activated mucosal T cells play a role in the pathogenesis of enteropathy in human small intestine. *J Exp Med.* 1988;167(4):1341-9.
27. Ferreira RC, Forsyth LE, Richman PI, Wells C, Spencer J, and MacDonald TT. Changes in the rate of crypt epithelial cell proliferation and mucosal morphology induced by a T-cell-mediated response in human small intestine. *Gastroenterology.* 1990;98(5 Pt 1):1255-63.
28. Bajaj-Elliott M, Poulsom R, Pender SL, Wathen NC, and MacDonald TT. Interactions between stromal cell--derived keratinocyte growth factor and epithelial transforming growth factor in immune-mediated crypt cell hyperplasia. *J Clin Invest.* 1998;102(8):1473-80.
29. MacDonald TT, Bajaj-Elliott M, and Pender SL. T cells orchestrate intestinal mucosal shape and integrity. *Immunol Today.* 1999;20(11):505-10.
30. Nordmann TM, Anderton H, Hasegawa A, Schweizer L, Zhang P, Stadler PC, et al. Spatial proteomics identifies JAKi as treatment for a lethal skin disease. *Nature.* 2024;635(8040):1001-9.
31. Johansen A, Sandve GKF, Ibsen JH, Lundin KEA, Sollid LM, and Stamnaes J. Biopsy proteome scoring to determine mucosal remodeling in celiac disease. *Gastroenterology.* 2024;167(3):493-504 e10.
32. Boehm U, Klamp T, Groot M, and Howard JC. Cellular responses to interferon-γ. *Annu Rev Immunol.* 1997;15:749-95.
33. Biton M, Haber AL, Rogel N, Burgin G, Beyaz S, Schnell A, et al. T helper cell cytokines modulate intestinal stem cell renewal and differentiation. *Cell.* 2018;175(5):1307-20 e22.
34. Ráki M, Tollefsen S, Molberg O, Lundin KE, Sollid LM, and Jahnsen FL. A unique dendritic cell subset accumulates in the celiac lesion and efficiently activates gluten-reactive T cells. *Gastroenterology.* 2006;131(2):428-38.
35. Wang F, Scoville D, He XC, Mahe MM, Box A, Perry JM, et al. Isolation and characterization of intestinal stem cells based on surface marker combinations and colony-formation assay. *Gastroenterology.* 2013;145(2):383-95 e1-21.
36. Guy-Grand D, DiSanto JP, Henchoz P, Malassis-Seris M, and Vassalli P. Small bowel enteropathy: role of intraepithelial lymphocytes and of cytokines (IL-12, IFN-γ, TNF) in the induction of epithelial cell death and renewal. *Eur J Immunol.* 1998;28(2):730-44.
37. Eriguchi Y, Nakamura K, Yokoi Y, Sugimoto R, Takahashi S, Hashimoto D, et al. Essential role of IFN-γ in T cell-associated intestinal inflammation. *JCI Insight.* 2018;3(18).
38. FitzPatrick MEB, Antanaviciute A, Dunstan M, Kunnapuu K, Trzupek D, Provine NM, et al. Immune-epithelial-stromal networks define the cellular ecosystem of the small intestine in celiac disease. *Nat Immunol.* 2025.
39. Dickson BC, Streutker CJ, and Chetty R. Coeliac disease: an update for pathologists. *J Clin Pathol.* 2006;59(10):1008-16.

40. Rahmani S, Galipeau HJ, Clarizio AV, Wang X, Hann A, Rueda GH, et al. Gluten-dependent activation of CD4^{+} T cells by MHC class II-expressing epithelium. *Gastroenterology.* 2024;167(6):1113-28.
41. Scott H, Sollid LM, Fausa O, Brandtzaeg P, and Thorsby E. Expression of major histocompatibility complex class II subregion products by jejunal epithelium in patients with coeliac disease. *Scand J Immunol.* 1987;26(5):563-71.
42. Kelly J, Weir DG, and Feighery C. Differential expression of HLA-D gene products in the normal and coeliac small bowel. *Tissue Antigens.* 1988;31(3):151-60.
43. Schweizer JJ, Mearin ML, Pena AS, Offerhaus GJ, Dreef EJ, Roep BO, et al. Expression of HLA-DQ antigens in the small-intestinal mucosa of patients with coeliac disease. *Scand J Gastroenterol.* 1991;26(6):605-10.
44. Sakai K, Takiguchi M, Mori S, Kobori O, Morioka Y, Inoko H, et al. Expression and function of class II antigens on gastric carcinoma cells and gastric epithelia: differential expression of DR, DQ, and DP antigens. *J Natl Cancer Inst.* 1987;79(5):923-32.
45. Liversidge JM, Sewell HF, and Forrester JV. Human retinal pigment epithelial cells differentially express MHC class II (HLA, DP, DR and DQ) antigens in response to *in vitro* stimulation with lymphokine or purified IFN-γ. *Clin Exp Immunol.* 1988;73(3):489-94.
46. Hoydahl LS, Richter L, Frick R, Snir O, Gunnarsen KS, Landsverk OJB, et al. Plasma cells are the most abundant gluten peptide MHC-expressing cells in inflamed intestinal tissues from patients with celiac disease. *Gastroenterology.* 2019;156(5):1428-39 e10.
47. Takashima S, Martin ML, Jansen SA, Fu Y, Bos J, Chandra D, et al. T cell-derived interferon-γ programs stem cell death in immune-mediated intestinal damage. *Sci Immunol.* 2019;4(42).
48. Takashima S, Sharma R, Chang W, Calafiore M, Fu YY, Jansen SA, et al. STAT1 regulates immune-mediated intestinal stem cell proliferation and epithelial regeneration. *Nat Commun.* 2025;16(1):138.
49. Omrani O, Krepelova A, Rasa SMM, Sirvinskas D, Lu J, Annunziata F, et al. IFNγ-Stat1 axis drives aging-associated loss of intestinal tissue homeostasis and regeneration. *Nat Commun.* 2023;14(1):6109.
50. Stamnaes J, Stray D, Stensland M, Sarna VK, Nyman TA, Lundin KEA, et al. In well-treated celiac patients low-level mucosal inflammation predicts response to 14-day gluten challenge. *Adv Sci (Weinh).* 2021;8(4):2003526.
51. Dotsenko V, Oittinen M, Taavela J, Popp A, Peraaho M, Staff S, et al. Genome-wide transcriptomic analysis of intestinal mucosa in celiac disease patients on a gluten-free diet and postgluten challenge. *Cell Mol Gastroenterol Hepatol.* 2021;11(1):13-32.
52. Raetz M, Hwang SH, Wilhelm CL, Kirkland D, Benson A, Sturge CR, et al. Parasite-induced TH1 cells and intestinal dysbiosis cooperate in IFN-γ-dependent elimination of Paneth cells. *Nat Immunol.* 2013;14(2):136-42.
53. Farin HF, Karthaus WR, Kujala P, Rakhshandehroo M, Schwank G, Vries RG, et al. Paneth cell extrusion and release of antimicrobial products is directly controlled by immune cell-derived IFN-γ. *J Exp Med.* 2014;211(7):1393-405.
54. Ward M, Ferguson A, and Eastwood MA. Jejunal lysozyme activity and the Paneth cell in coeliac disease. *Gut.* 1979;20(1):55-8.
55. Scott H, and Brandtzaeg P. Enumeration of Paneth cells in coeliac disease: comparison of conventional light microscopy and immunofluorescence staining for lysozyme. *Gut.* 1981;22(10):812-6.
56. Di Sabatino A, Miceli E, Dhaliwal W, Biancheri P, Salerno R, Cantoro L, et al. Distribution, proliferation, and function of Paneth cells in uncomplicated and complicated adult celiac disease. *Am J Clin Pathol.* 2008;130(1):34-42.
57. Cheng CW, Biton M, Haber AL, Gunduz N, Eng G, Gaynor LT, et al. Ketone body signaling mediates intestinal stem cell homeostasis and adaptation to diet. *Cell.* 2019;178(5):1115-31 e15.

58. Mihaylova MM, Cheng CW, Cao AQ, Tripathi S, Mana MD, Bauer-Rowe KE, et al. Fasting activates fatty acid oxidation to enhance intestinal stem cell function during homeostasis and aging. *Cell Stem Cell.* 2018;22(5):769-78 e4.
59. Gebert N, Cheng CW, Kirkpatrick JM, Di Fraia D, Yun J, Schadel P, et al. Region-specific proteome changes of the intestinal epithelium during aging and dietary restriction. *Cell Rep.* 2020;31(4):107565.
60. Beyaz S, Chung C, Mou H, Bauer-Rowe KE, Xifaras ME, Ergin I, et al. Dietary suppression of MHC class II expression in intestinal epithelial cells enhances intestinal tumorigenesis. *Cell Stem Cell.* 2021;28(11):1922-35 e5.
61. Fawkner-Corbett D, Antanaviciute A, Parikh K, Jagielowicz M, Geros AS, Gupta T, et al. Spatiotemporal analysis of human intestinal development at single-cell resolution. *Cell.* 2021;184(3):810-26 e23.
62. Beumer J, and Clevers H. Cell fate specification and differentiation in the adult mammalian intestine. *Nat Rev Mol Cell Biol.* 2021;22(1):39-53.
63. Mesin L, Di Niro R, Thompson KM, Lundin KE, and Sollid LM. Long-lived plasma cells from human small intestine biopsies secrete immunoglobulins for many weeks in vitro. *J Immunol.* 2011;187(6):2867-74.
64. Santos AJM, van Unen V, Lin Z, Chirieleison SM, Ha N, Batish A, et al. A human autoimmune organoid model reveals IL-7 function in coeliac disease. *Nature.* 2024;632(8024):401-10.
65. Lee SH, Carrero JA, Uppaluri R, White JM, Archambault JM, Lai KS, et al. Identifying the initiating events of anti-*Listeria* responses using mice with conditional loss of IFN-γ receptor subunit 1 (IFNGR1). *J Immunol.* 2013;191(8):4223-34.
66. Madison BB, Dunbar L, Qiao XT, Braunstein K, Braunstein E, and Gumucio DL. Cis elements of the villin gene control expression in restricted domains of the vertical (crypt) and horizontal (duodenum, cecum) axes of the intestine. *J Biol Chem.* 2002;277(36):33275-83.
67. Cox J, and Mann M. MaxQuant enables high peptide identification rates, individualized p.p.b.-range mass accuracies and proteome-wide protein quantification. *Nat Biotechnol.* 2008;26(12):1367-72.
68. Amundsen SF, Stamnaes J, Lundin KEA, and Sollid LM. Expression of transglutaminase 2 in human gut epithelial cells: Implications for coeliac disease. *PLoS One.* 2023;18(6):e0287662.
69. Tyanova S, Temu T, Sinitcyn P, Carlson A, Hein MY, Geiger T, et al. The Perseus computational platform for comprehensive analysis of (prote)omics data. *Nat Methods.* 2016;13(9):731-40.
70. Kong AT, Leprevost FV, Avtonomov DM, Mellacheruvu D, and Nesvizhskii AI. MSFragger: ultrafast and comprehensive peptide identification in mass spectrometry-based proteomics. *Nat Methods.* 2017;14(5):513-20.
71. Yu F, Haynes SE, Teo GC, Avtonomov DM, Polasky DA, and Nesvizhskii AI. Fast quantitative analysis of timsTOF PASEF data with MSFragger and IonQuant. *Mol Cell Proteomics.* 2020;19(9):1575-85.
72. Ritchie ME, Phipson B, Wu D, Hu Y, Law CW, Shi W, et al. limma powers differential expression analyses for RNA-sequencing and microarray studies. *Nucleic Acids Res.* 2015;43(7):e47.
73. Szklarczyk D, Kirsch R, Koutrouli M, Nastou K, Mehryary F, Hachilif R, et al. The STRING database in 2023: protein-protein association networks and functional enrichment analyses for any sequenced genome of interest. *Nucleic Acids Res.* 2023;51(D1):D638-D46.
74. Shannon P, Markiel A, Ozier O, Baliga NS, Wang JT, Ramage D, et al. Cytoscape: a software environment for integrated models of biomolecular interaction networks. *Genome Res.* 2003;13(11):2498-504.
75. Schindelin J, Arganda-Carreras I, Frise E, Kaynig V, Longair M, Pietzsch T, et al. Fiji: an open-source platform for biological-image analysis. *Nat Methods.* 2012;9(7):676-82.
76. Viken HD, Paulsen G, Sollid LM, Lundin KE, Tjonnfjord GE, Thorsby E, et al. Characterization of an HLA-DQ2-specific monoclonal antibody. Influence of amino acid substitutions in DQβ1*0202. *Hum Immunol.* 1995;42(4):319-27.

77. Perez-Riverol Y, Bandla C, Kundu DJ, Kamatchinathan S, Bai J, Hewapathirana S, et al. The PRIDE database at 20 years: 2025 update. *Nucleic Acids Res.* 2025;53(D1):D543-D53.

Figures and figure legends

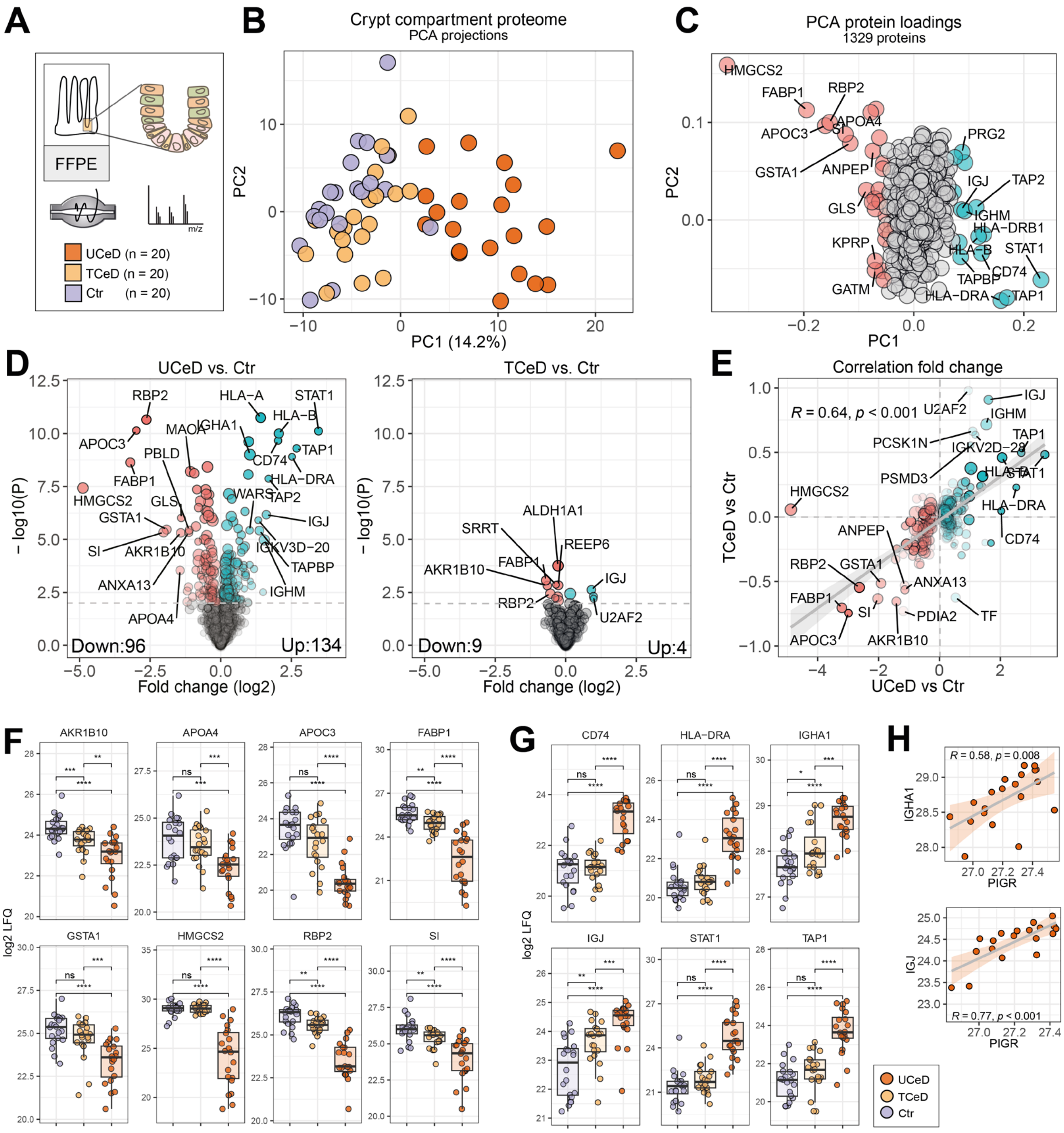

Figure 1. Small intestinal crypt proteome differs in untreated CeD as compared to treated CeD and non-CeD controls. (A) Schematic of the workflow for spatially resolved proteome analysis of the small intestinal crypt compartment from human FFPE duodenal biopsies. We analyzed biopsies from adults with CeD (n = 20) collected at the time of diagnosis (UCeD; untreated celiac disease) and after treatment with gluten free diet (TCeD; treated celiac disease), and biopsies from non-CeD subjects (Ctr) (n = 20). **(B)** Principal component analysis based on the expression of 1329 proteins. Each data point reflects averaged data per biopsy (n = 60). **(C)** Protein loadings that drive separation along PC1 and PC2. **(D-E)** Differential expression of proteins **(D)** in UCeD vs Ctr (left) and TCeD vs Ctr (right). Colored dots indicate significant DEPs comparing UCeD vs Ctr. **(E)** Correlation of log2-transformed fold change for UCeD vs Ctr DEP proteins (n = 230). Two-sample Students t-test, permutation-based false discovery rate (FDR) control (FDR = 0.05), 250 permutations was applied. R = Pearson's correlation coefficient. **(F, G)** Log2 LFQ protein expression values for selected proteins that drive PC1 and are DEP. Each dot reflects

mean expression per biopsy. *P* values determined using Mann-Whitney U test with Benjamin-Hochberg correction for multiple testing. ns: non-significant, * $P < 0.05$, ** $P < 0.01$, *** $P < 0.001$, **** $P < 0.0001$. **(H)** Correlation of log2-transformed LFQ protein expression. Each dot reflects average values for one biopsy. R = Pearson's correlation coefficient.

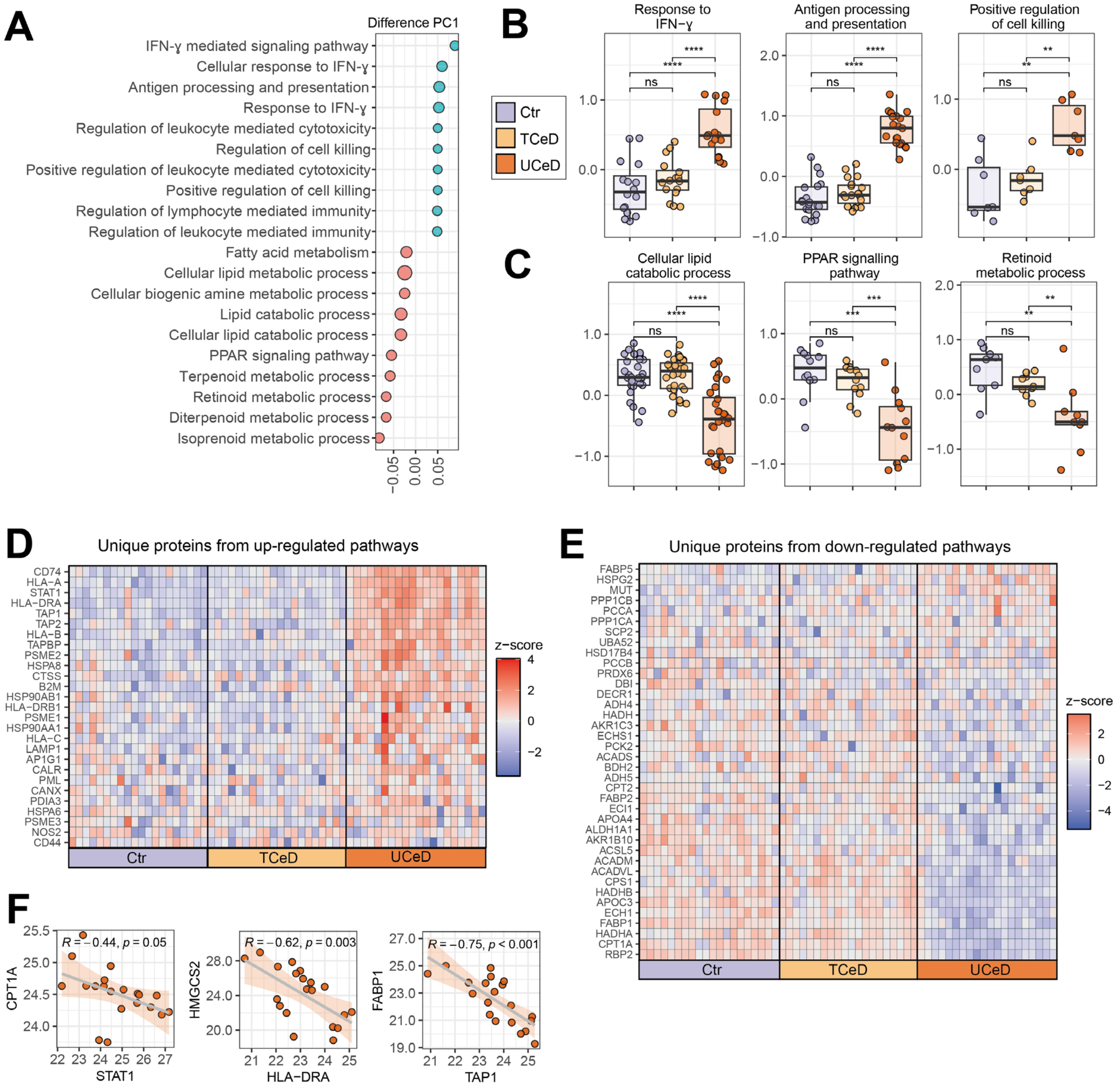

Figure 2. Altered biological pathways in crypt region of untreated CeD. (A) Top twenty most enriched Gene Ontology Biological Processes and KEGG pathways along PC1 from Fig. 1c. (Benjamin-Hochberg FDR <0.05). **(B, C)** Z-scored expression of proteins mapped to indicated enriched pathways. Each data point represents one protein and shows mean z-scored expression per group. *P* values determined using Mann-Whitney U test with Benjamin-Hochberg correction for multiple testing. ns: non-significant, * *P* < 0.05, ** *P* < 0.01, *** *P* < 0.001, **** *P* <0.0001. **(D, E)** Tile plot of z-scored protein expression for **(D)** unique proteins (n = 27) mapped to up-regulated pathways in (B) and (E) unique proteins (n = 38) mapped to up-regulated pathways in (C). **(F)** Correlation of log2-transformed LFQ protein expression. Each data point shows mean values for one biopsy. R = Pearson's correlation coefficient.

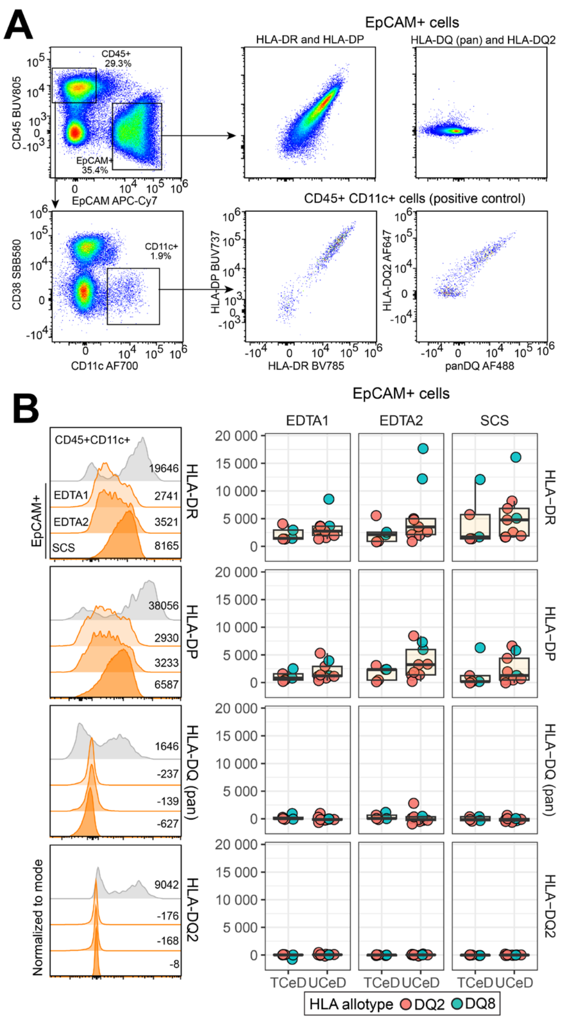

Figure 3. Expression of MHC II molecules on gut epithelial cells in CeD. (A) Flow cytometry plots with staining results for the collagenase-treated single cell suspension (SCS) fraction of an untreated CeD patient who is HLA-DQ2.5 homozygous. Cells expressing HLA-DQ in this subject should stain both for HLA-DQ (pan) and HLA-DQ2. **(B)** Staining results for HLA-DR, HLA-DP, HLA-DQ (pan) and HLA-DQ2 of three cell fractions – EDTA1, EDTA2 and SCS. The leftmost column gives histograms for the same subject as depicted in panel A, whereas the three other columns give staining results as median fluorescence intensity (MFI) of EpCAM+ cells of the three cell fractions from 9 UCeD and 5 TCeD subjects.

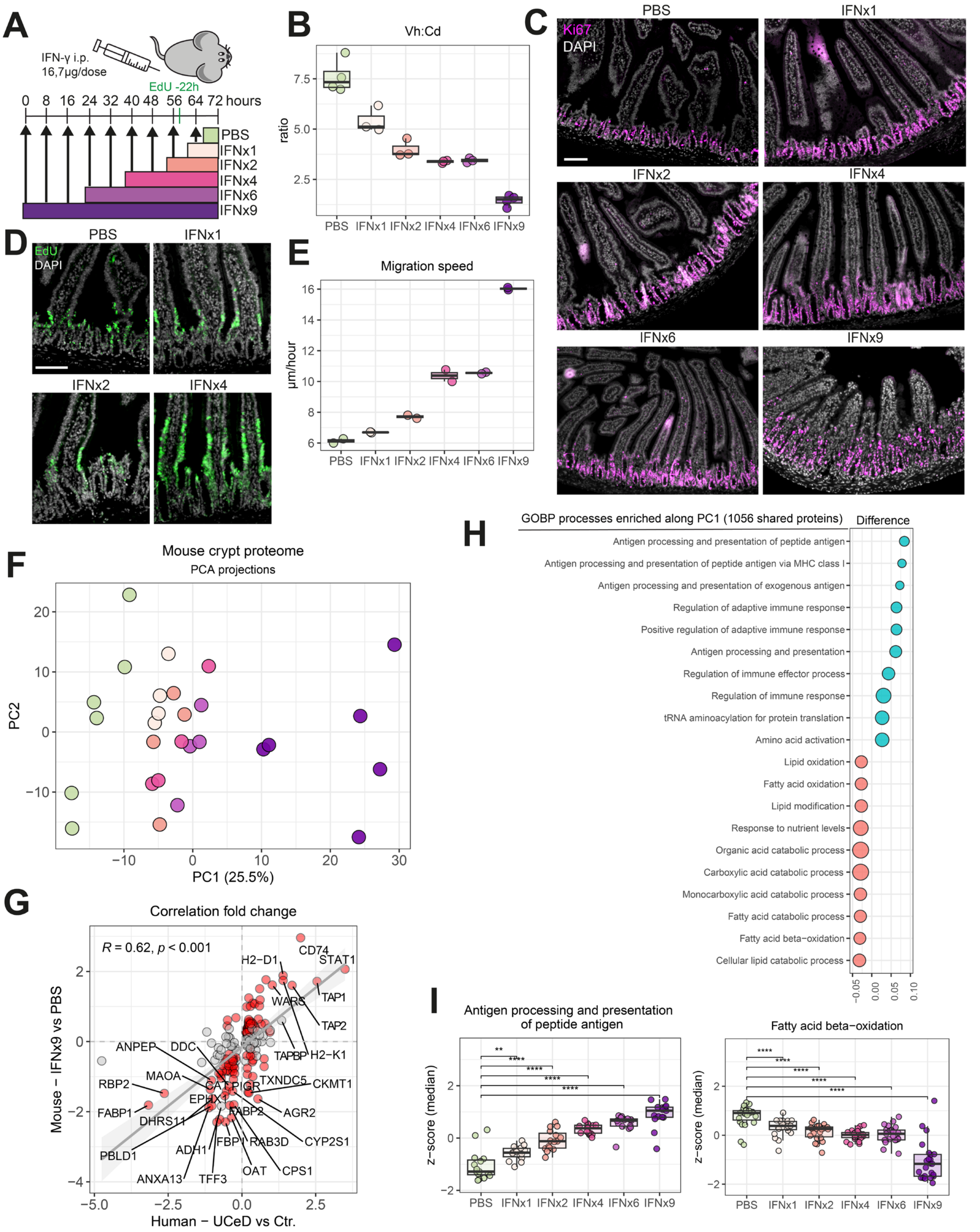

Figure 4. Small intestinal tissue remodeling induced by IFN-γ in mice. (A) Scheme depicting the IFN-γ injection regime. Mice were injected intraperitoneally at 8h intervals with 16.7µg IFN-γ in PBS or with PBS only, followed by euthanasia 8 hours after the last injection. A subset of the mice was injected with EdU 22 hours prior to euthanasia. **(B, C)** Measurement of villous height to crypt depth ratio **(B)** based on Ki67 staining **(C)** to define crypt depth and nuclei staining to define villous length. Each data point represents one mouse, data is pooled from three independent experiments. For each mouse, 3-6 pairs of villous height and crypt depths were measured per image from 3-5 separate images across the proximal small intestine. **(C)** Representative images of Ki67 staining are shown Scale bar, 100 µm. **(D, E)**

Assessment of cell migration rate from measurement of the EdU front **(D)** Representative images are shown. Scale bar, 100 µm. For PBS and IFNx4, the same sections are shown in (C) and in (D), staining for Ki67 and EdU respectively. **E)** Migration speed calculated from measurement of distance from crypt bottom to EdU migration front divided by 22h. Each data point represents one mouse, data is pooled from two independent experiments. For each mouse, 3-5 crypts were measured per image from 5-7 images across the proximal small intestine. Migration speed for IFNx9 reflects an approximation as EdU positive cells had reached the villous tip. **(F-I)** Crypt proteome analysis of proximal small intestine of IFN-γ treated mice. Principal component analysis (PCA) **(F)** based on expression of 3355 proteins. Each data point represents values averaged per mouse (n = 28). **(G)** Correlation of log2-transformed fold change for UCeD vs Ctr DEP proteins and mouse orthologs comparing IFNx9 vs PBS. R = Pearson's correlation coefficient. Colored dots reflect DEP for IFNx9 vs PBS (two-sample Student's *t* test). **(H)** Top twenty most enriched Gene Ontology Biological Processes along PC1 following filtering on proteins that are shared between mouse and human crypt proteome datasets (n = 1056). **(I)** Expression of proteins mapped to indicated enriched pathways. Each data point represents one protein and shows median z-scored expression per treatment group. *P* values determined using Mann-Whitney U test with Benjamin-Hochberg correction for multiple testing. * $P < 0.05$, ** $P < 0.01$, *** $P < 0.001$, **** $P < 0.0001$.

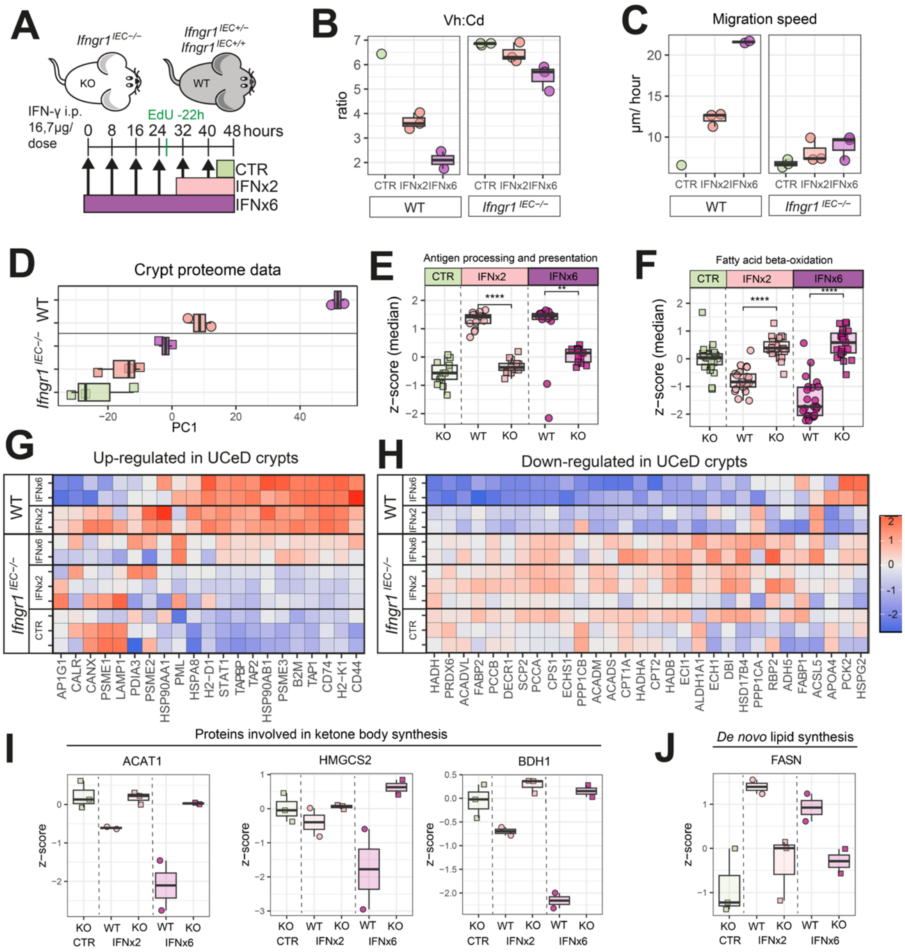

Figure 5. Small intestinal tissue remodeling induced by IFN-γ in mice with a targeted deletion of *Ifngr1* in intestinal epithelial cells. (A) Schematic depiction of IFN-γ injection regime for mice with deletion of *Ifngr1* (*Ifngr1*$^{\text{IEC}-/-}$; KO) in intestinal epithelial cells (IECs) and the corresponding littermate controls (wild type, WT). **(B, C)** Measurement of villous height to crypt depth (Vh:Cd) ratio and epithelial cell migration speed based on EdU staining. For IFNx6 WT mice, the EdU migration front had reached the villi tips. **(D)** Crypt proteome analysis reveals separation of samples along PC1 according to *Ifngr1* status and IFN-γ injection. Each data point reflects one mouse. **(E, F)** Expression of proteins mapped to indicated pathways. Each data point represents one protein and shows median z-scored expression per group. *P* values determined using Mann-Whitney U test with Benjamin-Hochberg correction for multiple testing * *P* < 0.05, ** *P* < 0.01, *** *P* < 0.001, **** *P* <0.0001. **(G, H)** Tile plot of z-scored expression of proteins from pathways **(G)** upregulated in UCeD (Fig. 2D; n = 21 mouse orthologs) and **(H)** downregulated in UCeD (Fig. 2E; n = 30 mouse orthologs). **(I, J)**, Expression (z-scored) of selected proteins involved in ketone body synthesis **(I)** and FASN involved in *de novo* lipid synthesis **(J)**. Each data point reflects one mouse.

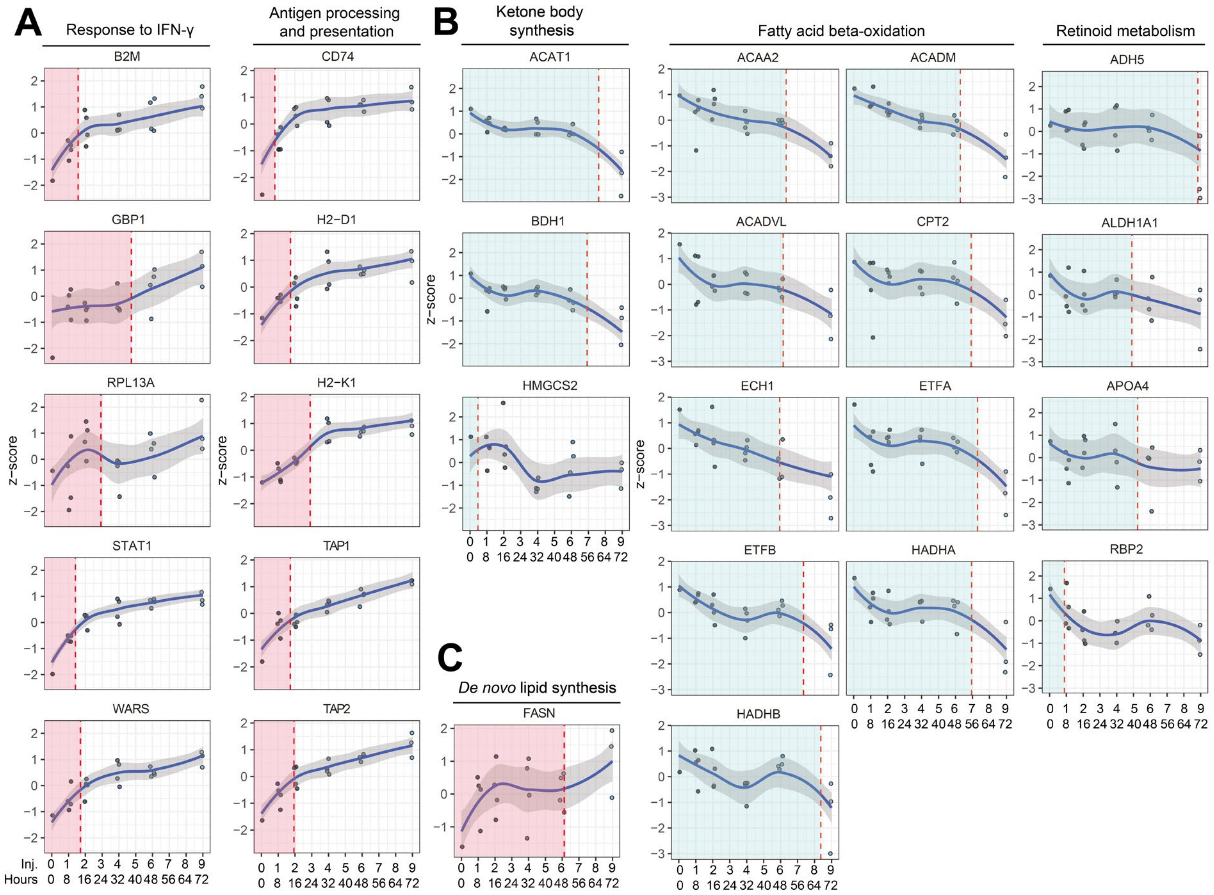

Figure 6. Kinetics of IFN-γ driven alterations in proteomic signatures of crypt region cells of mice. Time and IFN-γ dose-dependent increase (**A, C**) or decrease **(B)** in mouse crypt expression of proteins that represent selected GO Biological Processes that are altered in UCeD crypts. Each data point reflects one mouse. Smoothed curves were generated using LOESS regression (blue line). Shaded regions represent 95 % confidence intervals for the fitted curve. Vertical line (red) indicates the model point at 50 % change in protein expression. Colors indicate proteins that increase (light red) or decrease (light blue) in response to IFN-γ.